Topological Exciton Bands in Moiré Heterojunctions

Fengcheng Wu, Timothy Lovorn, and A. H. MacDonald

Phys. Rev. Lett. **118**, 147401 — Published 5 April 2017

DOI: 10.1103/PhysRevLett.118.147401

Topological Exciton Bands in Moiré Heterojunctions

Fengcheng Wu,[1,2] Timothy Lovorn,[1] and A. H. MacDonald[1]

[1] *Department of Physics, University of Texas at Austin, Austin, TX 78712, USA*
[2] *Materials Science Division, Argonne National Laboratory, Argonne, IL 60439, USA*

(Dated: February 24, 2017)

Moiré patterns are common in van der Waals heterostructures and can be used to apply periodic potentials to elementary excitations. We show that the optical absorption spectrum of transition metal dichalcogenide bilayers is profoundly altered by long period moiré patterns that introduce twist-angle dependent satellite excitonic peaks. Topological exciton bands with non-zero Chern numbers that support chiral excitonic edge states can be engineered by combining three ingredients: i) the valley Berry phase induced by electron-hole exchange interactions, ii) the moiré potential, and iii) the valley Zeeman field.

PACS numbers: 71.35.-y, 74.78.Fk, 78.67.-n, 03.65.Vf

Stacking two-dimensional (2D) materials into van der Waals heterostructures opens up new strategies for materials property engineering. One increasingly important example is the possibility of using the relative orientation (twist) angle between two 2D crystals to tune electronic properties. For small twist angles and lattice-constant mismatches, heterostructures exhibit long period moiré patterns that can yield dramatic changes. Moiré pattern formed in graphene-based heterostructures has been extensively studied, and many interesting phenomena have been observed, for example gap opening at graphene's Dirac point [1, 2], generation of secondary Dirac points[3, 4] and Hofstadter-butterfly spectra in a strong magnetic field[1, 5, 6].

In this Letter, we study the influence of moiré patterns on collective excitations, focusing on the important case of excitons in the transition metal dichalcogenide (TMD) 2D semiconductors [7, 8] like MoS_2 and WS_2. Exciton features dominate the optical response of these materials because electron-hole pairs are strongly bound by the Coulomb interaction [9–12]. An exciton inherits a pseudospin-1/2 valley degree of freedom from its constituent electron and hole, and the exciton valley pseudospin can be optically addressed [13–16], providing access to the valley Hall effect [17] and the valley selective optical Stark effect [18, 19].

As in the case of graphene/hexagonal boron nitride and graphene/graphene, a moiré pattern can be established in TMD bilayers by using two different materials with a small lattice mismatch, by applying a small twist, or by combining both effects. TMD heterostructures have been realized [20–22] experimentally and can host interesting effects, for example the observation of valley polarized interlayer excitons with long lifetimes [23], the theoretical prediction of multiply degenerate interlayer excitons [24], and the possibility of achieving spatially indirect exciton condensation [25, 26]. Our focus here is instead on the *intralayer* excitons that are more strongly coupled to light. As we explain below, the moiré pattern produces a periodic potential, mixing momentum states separated by moiré reciprocal lattice vectors and producing satellite optical absorption peaks that are revealing. The exciton energy-momentum dispersion can be measured by tracking the dependence of satellite peak energies on twist angle.

The valley pseudospin of an exciton is intrinsically coupled to its center-of-mass motion by the electron-hole exchange interaction[27–30]. This effective spin-orbit coupling endows the exciton with a 2π momentum-space Berry phase[31]. We show that topological exciton bands characterized by quantized Chern numbers can be achieved by exploiting this momentum-space Berry phase combined with a periodic potential due to the moiré pattern and time-reversal symmetry breaking by a Zeeman field. All three ingredients are readily available in TMD bilayers. The bulk topological bands lead to chiral edge states, which can support unidirectional transport of excitons optically generated on the edge. Our study therefore suggests a practical new route to engineer topological collective excitations which are now actively sought[32–37] in several different contexts.

Exciton Potential Energy— For definiteness we consider the common chalcogen TMD bilayer MoX_2/WX_2 with a small twist angle θ and an in-plane displacement $\boldsymbol{d}$. TMDs with a common chalcogen (X) atom have small lattice mismatches ($\sim 0.1\%$), which we neglect to simplify calculations. Because of the van der Waals heterojunction character and relative band offsets, both conduction and valence bands of MoX_2 and WX_2 are weakly coupled across the heterojunction. The heterojunctions have two distinct stacking orders AA and AB, which are illustrated in Figs. 1(a) and 1(d). Both configurations have been experimentally realized [23, 38].

We start by analyzing the bilayer electronic structure at zero twist angle. Fully-relativistic density-functional-theory *ab initio* calculation is performed for crystalline MoS_2/WS_2 ($\theta = 0°$) as a function of relative displacement $\boldsymbol{d}$. We used the local density approximation with optimized norm-conserving pseudopotentials [39, 40] as implemented in Quantum Espresso [41], and determined

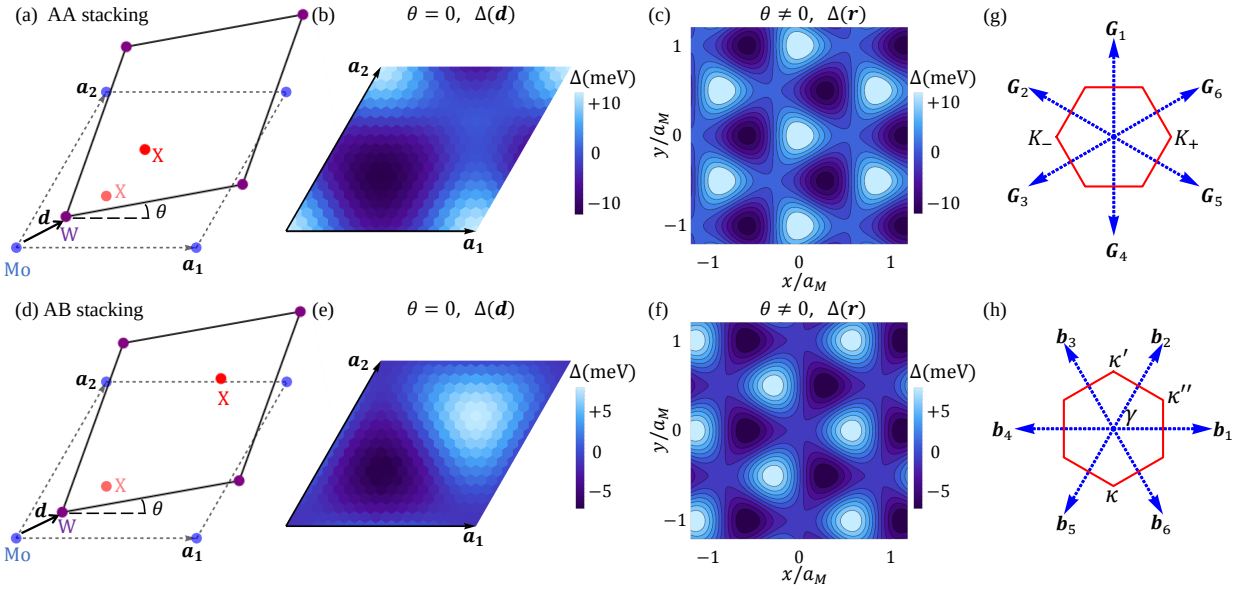

FIG. 1. (color online). (a) Illustration of AA stacking with a small twist angle θ and an in-plane displacement $\boldsymbol{d}$. (b) Variation of MoS_2 band gap as a function of $\boldsymbol{d}$ in AA stacked MoS_2/WS_2 bilayer with zero twist angle. (c) Variation of MoS_2 band gap as a function of position in AA stacked twisted MoS_2/WS_2. (d)-(f) Corresponding plots for AB stacking. (g) First-shell reciprocal lattice vectors $\boldsymbol{G}_j$ of a monolayer TMD triangular lattice and the corresponding Brillouin zone (red hexagon). (h) Moiré reciprocal lattice vectors and corresponding Brillouin zone

the orbital character of electronic bands using Wannier90 [42]. More details of the calculation are presented in the Supplemental Material [43]. Our primary interest here is intra-layer physics. Figs. 1(b) and 1(e) illustrate the $\boldsymbol{d}$ dependence of the energy gap at the $K_\pm$ points between states concentrated in the MoS_2 layer. The variation of the gap is a periodic function of $\boldsymbol{d}$ with the 2D lattice periodicity, and is adequately approximated by the lowest harmonic expansion:

$$\Delta(\boldsymbol{d}) \equiv E_g(\boldsymbol{d}) - \langle E_g \rangle \approx \sum_{j=1}^{6} V_j \exp(i\boldsymbol{G}_j \cdot \boldsymbol{d}), \quad (1)$$

where E_g is the intralayer band gap of MoS_2, $\langle E_g \rangle$ is its average over $\boldsymbol{d}$, and $\boldsymbol{G}_j$ is a one of the first-shell reciprocal lattice vectors illustrated in Fig. 1(g). Three-fold rotational symmetry of the lattice leads to the constraint:

$$V_1 = V_3 = V_5,\ V_2 = V_4 = V_6. \quad (2)$$

Because Δ is real, we also have that $V_1 = V_4^*$. It follows that all six V_j are fixed by $V_1 = V\exp(i\psi)$. For MoS_2 on WS_2 we find that $(V, \psi) = (2.3\text{meV}, 30.8^\circ)$ for AA stacking and $(1.4\text{meV}, 98.6^\circ)$ for AB stacking. Because the band offset between the two layers can be modified by external electric fields, we expect that the values of these parameters can be tuned using gate voltages.

Rotation by angle θ transforms lattice vector $\boldsymbol{L}$ to $\boldsymbol{L}' = \mathcal{R}(\theta)\boldsymbol{L}$, where $\mathcal{R}(\theta)$ is the rotation matrix. For small twist angles, the relative displacement[44] between two layers near position $\boldsymbol{L}'$ is therefore,

$$\boldsymbol{d}(\boldsymbol{L}') = \hat{T}\boldsymbol{L}' = \hat{T}(\boldsymbol{L}' - \boldsymbol{L}) \approx \hat{T}(\theta\hat{z} \times \boldsymbol{L}'), \quad (3)$$

where the operator $\hat{T}$ reduces a vector to the Wigner-Seitz cell of the triangular lattice labeled by $\boldsymbol{L}$. In the limit of small θ, the displacement varies smoothly with position. Because the size of an exciton in TMDs ($\sim$ 1nm) is larger than the lattice constant scale, validating a $k \cdot p$ description, but much smaller than moiré periods, the influence of the displacement on exciton energy is local [45, 46]. We find that the variation in the band gap dominates over that of the binding energy[43]. For simplicity, we assume that the variation of exciton energy will follow that of local band gap:

$$\begin{aligned}\Delta(\boldsymbol{r}) &\approx \Delta(\boldsymbol{d}(\boldsymbol{r})) \approx \sum_{j=1}^{6} V_j \exp(i\boldsymbol{G}_j \cdot \boldsymbol{d}(\boldsymbol{r})) \\ &\approx \sum_{j=1}^{6} V_j \exp(i\boldsymbol{G}_j \cdot (\theta\hat{z} \times \boldsymbol{r})) = \sum_{j=1}^{6} V_j \exp(i\boldsymbol{b}_j \cdot \boldsymbol{r}).\end{aligned} \quad (4)$$

Here $\Delta(\boldsymbol{r})$ acts as an exciton potential energy, and $\boldsymbol{b}_j = \theta\boldsymbol{G}_j \times \hat{z}$ defines the reciprocal lattice vectors of the moiré pattern. The band gap varies periodically in space due to the moiré pattern, as illustrated in Figs. 1(c) and 1(f). The moiré periodicity a_M is controlled by the twist angle: $a_M \approx a_0/\theta$, where a_0 is the lattice constant of a monolayer TMD.

Optical response.— We study the A exciton, the lowest-energy bright exciton, in monolayer MoS_2. Its low-energy

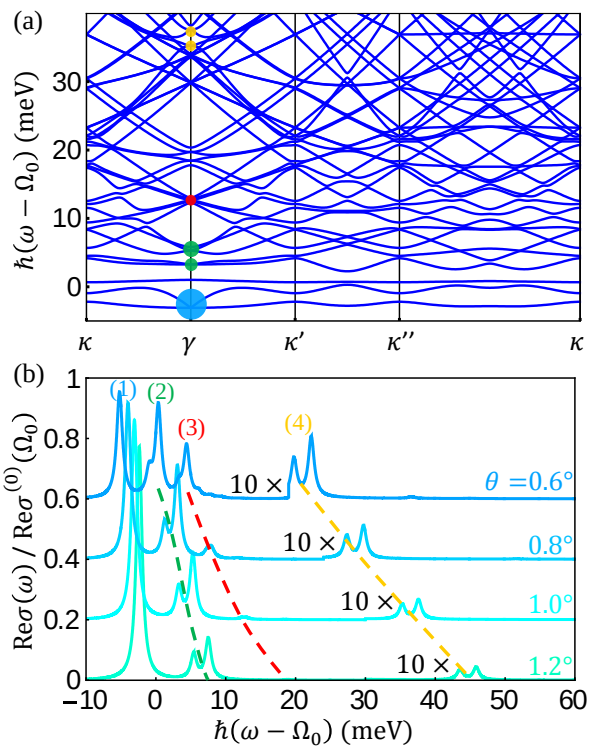

FIG. 2. (color online). (a) Exciton moiré bands along paths connecting high symmetry points in the MBZ. The twist angle θ used for this calculation is 1°. The sizes of the dots at the γ point correspond to the weight of state $|K_\pm^{(0)}\rangle$. The color of the dots encodes the main character of the states, with blue, red, green and yellow corresponding to character (1), (2), (3) and (4). See text. (b) Optical conductivity at several twist angles θ. Curves for different θ are shifted vertically for clarity and the dashed curves track the peak evolution. The two mini-peaks in (4) are amplified ten times. The broadening factor η is taken to be 0.5meV. The exciton potential parameters of AA stacked MoS_2/WS_2 were used in these calculations.

effective Hamiltonian [27–30] is:

$$H_0 = (\hbar\Omega_0 + \frac{\hbar^2\boldsymbol{Q}^2}{2M})\tau_0 + J|\boldsymbol{Q}|\tau_0 + J|\boldsymbol{Q}|\big[\cos(2\phi_{\boldsymbol{Q}})\tau_x + \sin(2\phi_{\boldsymbol{Q}})\tau_y\big], \quad (5)$$

where $\boldsymbol{Q}$ is exciton momentum, $\hbar\Omega_0$ is its $\boldsymbol{Q}=0$ energy, $\hbar^2\boldsymbol{Q}^2/(2M)$ is its center-of-mass kinetic energy, and τ_0 and $\tau_{x,y}$ are respectively identity matrix and Pauli matrices in valley space. In Eq. (5), $\phi_{\boldsymbol{Q}}$ is the orientation angle of the 2D vector $\boldsymbol{Q}$, $J|\boldsymbol{Q}|\tau_0$ accounts for intravalley electron-hole exchange interactions, and the $\tau_{x,y}$ terms account for their intervalley counterparts[47]. It follows that the A exciton has two energy modes,

$$E_\pm(\boldsymbol{Q}) = \hbar\Omega_0 + \frac{\hbar^2\boldsymbol{Q}^2}{2M} + J|\boldsymbol{Q}| \pm J|\boldsymbol{Q}|. \quad (6)$$

Note that E_+ has linear dispersion at small $|\boldsymbol{Q}|$, while the lower mode E_- is quadratic. From the *ab initio* GW Bethe-Salpeter calculation of Ref. [48] we obtain $M = 1.3m_0$ and $J = 0.4\text{eV}\cdot\text{Å}$, where m_0 is the free electron mass. Since the gap variation is guaranteed by time reversal symmetry to be identical for K_+ and K_- valleys, the exciton effective Hamiltonian of twisted bilayers is $H = H_0 + \Delta(\boldsymbol{r})\tau_0$.

We numerically diagonalize the Hamiltonian matrix using a plane-wave expansion; exciton momentum reduced to the moiré Brillouin zone (MBZ) is a good quantum number. Fig. 2(a) illustrates the MoS_2 A exciton moiré bands for a 1° twist relative to WS_2. Smaller twist angles imply smaller MBZ dimensions and more moiré bands in a given energy window. For twist angles $\theta > 0.5°$, the wavelength (640nm) of light that excites A excitons greatly exceeds the moiré periodicity (<36nm). It follows that only excitons close to the MBZ center γ are optically active. The real part of the optical conductivity can be expressed as follows,

$$\begin{aligned}\text{Re}\sigma(\omega) &= \frac{1}{\omega\mathcal{A}}\sum_n \big|\langle\chi_n|j_x|G\rangle\big|^2\Gamma_1(\omega-\omega_n)\\ &\approx \frac{\big|\langle K_+^{(0)}|j_x|G\rangle\big|^2}{\omega\mathcal{A}}\sum_n\Big|\sum_{\alpha=\pm}\langle\chi_n|K_\alpha^{(0)}\rangle\Big|^2\Gamma_1(\omega-\omega_n) \quad (7)\\ &\approx \frac{1}{2}\text{Re}\sigma^{(0)}(\Omega_0)\sum_n\Big|\sum_{\alpha=\pm}\langle\chi_n|K_\alpha^{(0)}\rangle\Big|^2\Gamma_2(\omega-\omega_n),\end{aligned}$$

where $\mathcal{A}$ is the system area, $\Gamma_m(\omega-\omega_n) = \eta^m/\big[\hbar^2(\omega-\omega_n)^2+\eta^2\big]$ and η is a broadening parameter. In Eq. (7) j_x is the current operator, $|G\rangle$ is the neutral semiconductor ground state, $|\chi_n\rangle$ and $\hbar\omega_n$ are the eigenstates and eigenvalues of the exciton moiré Hamiltonian at the γ point, $|K_\alpha^{(0)}\rangle$ is the valley K_α exciton eigenstate at zero twist angle, and $\text{Re}\sigma^{(0)}(\Omega_0)$ is the A exciton optical conductivity peak also at zero twist angle. The assumption underlying Eq. (7) is that only the $|K_\pm^{(0)}\rangle$ component in $|\chi_n\rangle$ contributes to the optical response. The final form for $\sigma(\omega)$ emphasizes that the exciton moiré potential has the effect of redistributing the A-exciton peak over a series of closely spaced sub-peaks.

Theoretical optical conductivities for a series of twist angles are illustrated in Fig. 2(b). Peaks labelled (1-4) (see caption) correspond respectively to bare excitons at zero momentum, E_- excitons at momentum $\boldsymbol{b}_i$, E_- excitons at momentum $\sqrt{3}\boldsymbol{b}_i\times\hat{z}$, and E_+ excitons at momentum $\boldsymbol{b}_i$. Without the moiré pattern there would only be one peak centered around frequency Ω_0; umklapp scattering off the moiré potentials unveils the formerly dark finite-momentum excitonic states. Both (2) and (4) give rise to two mini-peaks with a small energy splitting. As the twist angle decreases, $|\boldsymbol{b}_i|$ is reduced and the satellite peaks shift to lower energy and become stronger; for $\theta\sim 0.6°$ satellite peaks (2) and (3) have strength that is comparable to that of peak (1). Although peak (4) is weak, it decays more slowly compared to peak (3) when θ increases. The energy difference between peak (2) and

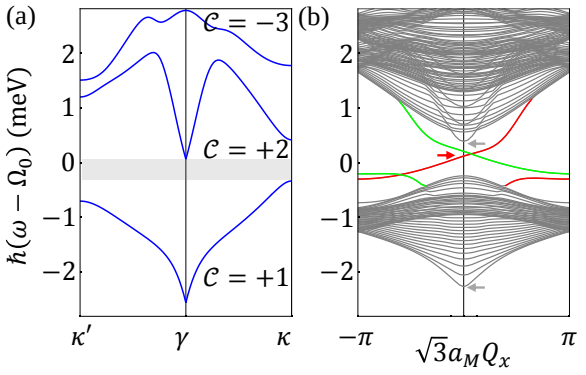

FIG. 3. (color online). (a) Topological exciton bands with quantized Chern numbers $\mathcal{C}$ for twist angle $\theta = 1^\circ$. The gray bar identifies the gap between the first and second exciton moiré band. (b) Stripe geometry quasi-1D bands for the same twist angle, an extended edge along the x direction, and finite width in the y direction. The red and green lines show the dispersions of chiral exciton states that are localized on opposite edges of the stripe. In (a) and (b), h_z is 1.5meV, and (V, ψ) take the parameter values of AB stacked MoS_2/WS_2.

(4) provides a direct measurement of the electron-hole exchange interaction strength.

Topological excitons.—The intervalley exchange interaction acts as an in-plane valley-space pseudo-magnetic field which rotates by 4π when the momentum encloses its origin once. This non-trivial winding number can be used to engineer topological exciton bands when combined with the moiré superlattice potential , which provides a finite Brillouin zone and an energy gap above the lowest exciton band at every $\boldsymbol{Q}$ point in the MBZ except the γ point. An external Zeeman term $h_z\tau_z$ can split the degeneracy at γ. A Zeeman term of this form has been experimentally realized in monolayer TMDs by applying a magnetic field [49–51] and by using a valley selective optical Stark effect [18, 19]. The topology of the exciton bands is characterized by Berry curvature $\mathcal{F}$ and Chern number $\mathcal{C}$, just as in the electronic case:

$$\mathcal{F}_n(\boldsymbol{Q}) = \hat{z}\cdot\nabla_{\boldsymbol{Q}}\times\left[i\langle\chi_n(\boldsymbol{Q})|\nabla_{\boldsymbol{Q}}|\chi_n(\boldsymbol{Q})\rangle\right],$$
$$\mathcal{C}_n = \int_{\mathrm{MBZ}}\frac{d^2\boldsymbol{Q}}{2\pi}\mathcal{F}_n(\boldsymbol{Q}), \tag{8}$$

where $|\chi_n(\boldsymbol{Q})\rangle$ represents the nth eigenstate of Hamiltonian H at momentum $\boldsymbol{Q}$. Fig. 3(a) presents our results for the topological properties of moiré exciton bands in AB stacked MoS_2/WS_2. We find that the first exciton band can possess a non-zero Chern number, and that it is isolated from other bands by a global energy gap. The corresponding Berry curvature $\mathcal{F}$ has hot spots around γ, κ, and κ' points in the MBZ. $\mathcal{F}$ around γ is simply understood in terms of the valley Berry phase induced by the exchange interaction, and its sign is determined by that of h_z. The peak in $\mathcal{F}$ around the κ and κ' point is related to gap opening due to moiré pattern, and can vary as a function of ψ, the phase of V_1. We find that the Chern number is finite in a large parameter space of (ψ, θ)[43]. Therefor we expect that topological exciton bands appear routinely in TMD bilayers.

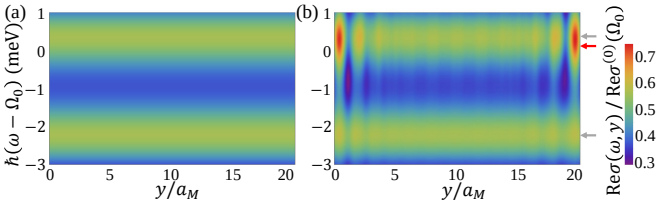

FIG. 4. (color online). Spatially resolved optical conductivity on the same stripe geometry as studied in Fig. 3(b). The optical conductivity is averaged over x. (a) Response from bulk states. The energy splitting between the two peaks is due to the Zeeman energy. An energy broadening factor of 1meV is used. (b) Response from both bulk and edge states. There is an enhancement of the optical response around the edge due to edge states. The arrows indicate the energy level of bulk states (gray arrow) and edge state (red arrow) in the absence of energy broadening, and correspond to the three arrows shown in Fig. 3(b).

Chiral excitonic edge states expected for topological bands is confirmed by studying the energy spectrum of a finite-width stripe [43], as illustrated in Fig. 3(b). These states can support unidirectional excitonic transport channel. We have computed optical response of the edge states[43]. The spatially resolved optical conductivity is shown in Fig. 4. Based on numerical results, we find that the *maximum* local optical conductivity due to one edge state is about $0.19\mathrm{Re}\sigma^{(0)}(\Omega_0)$, which is comparable in magnitude to that of the bulk states. As illustrated in Fig. 4(b), edge states give rise to enhanced response around the edge, and therefore can be detected by spatially resolved absorption spectroscopy.

In summary, intralayer excitons in a twisted TMD bilayer exhibit rich phenomena enabled by the moiré pattern, including satellite excitonic peaks in optical absorption peaks that are tunable by varying twist angle. The moiré superlattice potential, the exciton Zeeman field, and the electron-hole exchange induced valley Berry phase can in combination give rise to topological exciton bands. Our analysis points to a practical strategy to realize topological excitons.

We would like to thank Feng Wang and Ivar Martin for useful discussions. Work at Austin was supported by the Department of Energy, Office of Basic Energy Sciences under contract DE-FG02-ER45118 and award # DE-SC0012670, and by the Welch foundation under grant TBF1473. Work of FW at Argonne was supported by the Department of Energy, Office of Science, Materials Sciences and Engineering Division. We acknowledge computer time allocations from Texas Advanced Computing Center.

[1] B. Hunt *et al.*, Science **340**, 1427 (2013).
[2] E. Wang *et al.*, Nat. Phys. **12**, 1111 (2016).
[3] M. Yankowitz, J. Xue, D. Cormode, J. D. Sanchez-Yamagishi, K. Watanabe, T. Taniguchi, P. Jarillo-Herrero, P. Jacquod, and B. J. LeRoy, Nat. Phys. **8**, 382 (2012).
[4] L. Ponomarenko *et al.*, Nature **497**, 594 (2013).
[5] C. Dean *et al.*, Nature **497**, 598 (2013).
[6] K. Kim, A. DaSilva, S. Huang, B. Fallahazad, S. Larentis, T. Taniguchi, K. Watanabe, B. J. LeRoy, A. H. MacDonald, and E. Tutuc, submitted.
[7] A. Splendiani, L. Sun, Y. Zhang, T. Li, J. Kim, C.-Y. Chim, G. Galli, and F. Wang, Nano Lett. **10**, 1271 (2010).
[8] K. F. Mak, C. Lee, J. Hone, J. Shan, and T. F. Heinz, Phys. Rev. Lett. **105**, 136805 (2010).
[9] Z. Ye, T. Cao, K. OBrien, H. Zhu, X. Yin, Y. Wang, S. G. Louie, and X. Zhang, Nature **513**, 214 (2014).
[10] K. He, N. Kumar, L. Zhao, Z. Wang, K. F. Mak, H. Zhao, and J. Shan, Phys. Rev. Lett. **113**, 026803 (2014).
[11] A. Chernikov, T. C. Berkelbach, H. M. Hill, A. Rigosi, Y. Li, O. B. Aslan, D. R. Reichman, M. S. Hybertsen, and T. F. Heinz, Phys. Rev. Lett. **113**, 076802 (2014).
[12] D. Y. Qiu, F. H. da Jornada, and S. G. Louie, Phys. Rev. Lett. **111**, 216805 (2013).
[13] T. Cao, G. Wang, W. Han, H. Ye, C. Zhu, J. Shi, Q. Niu, P. Tan, E. Wang, B. Liu, *et al.*, Nat. Commun. **3**, 887 (2012).
[14] H. Zeng, J. Dai, W. Yao, D. Xiao, and X. Cui, Nat. Nanotechnol. **7**, 490 (2012).
[15] K. F. Mak, K. He, J. Shan, and T. F. Heinz, Nat. Nanotechnol. **7**, 494 (2012).
[16] D. Xiao, G.-B. Liu, W. Feng, X. Xu, and W. Yao, Phys. Rev. Lett. **108**, 196802 (2012).
[17] K. F. Mak, K. L. McGill, J. Park, and P. L. McEuen, Science **344**, 1489 (2014).
[18] J. Kim, X. Hong, C. Jin, S.-F. Shi, C.-Y. S. Chang, M.-H. Chiu, L.-J. Li, and F. Wang, Science **346**, 1205 (2014).
[19] E. J. Sie, J. W. McIver, Y.-H. Lee, L. Fu, J. Kong, and N. Gedik, Nat. Mat. **14**, 290 (2015).
[20] H. Fang *et al.*, PNAS **111**, 6198 (2014).
[21] Y. Gong *et al.*, Nat. Mat. **13**, 1135 (2014).
[22] K. Liu, L. Zhang, T. Cao, C. Jin, D. Qiu, Q. Zhou, A. Zettl, P. Yang, S. G. Louie, and F. Wang, Nat. Commun. **5**, 4966 (2014).
[23] P. Rivera, K. L. Seyler, H. Yu, J. R. Schaibley, J. Yan, D. G. Mandrus, W. Yao, and X. Xu, Science **351**, 688 (2016).
[24] H. Yu, Y. Wang, Q. Tong, X. Xu, and W. Yao, Phys. Rev. Lett. **115**, 187002 (2015).
[25] M. Fogler, L. Butov, and K. Novoselov, Nat. Commun. **5** (2014).
[26] F.-C. Wu, F. Xue, and A. H. MacDonald, Phys. Rev. B **92**, 165121 (2015).
[27] H. Yu, G.-B. Liu, P. Gong, X. Xu, and W. Yao, Nat. Commun. **5** (2014).
[28] M. M. Glazov, T. Amand, X. Marie, D. Lagarde, L. Bouet, and B. Urbaszek, Phys. Rev. B **89**, 201302 (2014).
[29] T. Yu and M. W. Wu, Phys. Rev. B **89**, 205303 (2014).
[30] F. Wu, F. Qu, and A. H. MacDonald, Phys. Rev. B **91**, 075310 (2015).
[31] The effect of the exchange interaction on spatially indirect excitons has been discussed, for example, in Ref. [52].
[32] J. Yuen-Zhou, S. K. Saikin, N. Y. Yao, and A. Aspuru-Guzik, Nat. Mat. **13**, 1026 (2014).
[33] T. Karzig, C.-E. Bardyn, N. H. Lindner, and G. Refael, Phys. Rev. X **5**, 031001 (2015).
[34] C.-E. Bardyn, T. Karzig, G. Refael, and T. C. H. Liew, Phys. Rev. B **91**, 161413 (2015).
[35] A. V. Nalitov, D. D. Solnyshkov, and G. Malpuech, Phys. Rev. Lett. **114**, 116401 (2015).
[36] J. C. W. Song and M. S. Rudner, PNAS **113**, 4658 (2016).
[37] D. Jin, L. Lu, Z. Wang, C. Fang, J. D. Joannopoulos, M. Soljačić, L. Fu, and N. X. Fang, Nat. Commun. **7**, 13486 (2016).
[38] N. R. Wilson *et al.*, Sci. Adv. **3**, e1601832 (2017).
[39] D. R. Hamann, Phys. Rev. B **88**, 085117 (2013).
[40] M. Schlipf and F. Gygi, Comput. Phys. Commun. **196**, 36 (2015).
[41] P. Giannozzi *et al.*, J. Phys.: Condens. Matter **21**, 395502 (2009).
[42] A. A. Mostofi, J. R. Yates, G. Pizzi, Y.-S. Lee, I. Souza, D. Vanderbilt, and N. Marzari, Comput. Phys. Commun. **185**, 2309 (2014).
[43] See Supplemental Material at http://link.aps.org/supplemental for details of *ab initio* calculations, discussion on local approximation, topological phase diagram and edge state analysis. It includes Refs. [53–56].
[44] Bulk properties of moiré systems with finite twist angle are independent of the relative displacement prior to twist which we set to zero. See Ref. 57 for an explanation.
[45] M. Wu, X. Qian, and J. Li, Nano Lett. **14**, 5350 (2014).
[46] J. Jung, A. Raoux, Z. Qiao, and A. H. MacDonald, Phys. Rev. B **89**, 205414 (2014).
[47] We used static approximation for the exchange interaction. Retardation effect results in intrinsic energy broadening of exciton states in the light cone. See Ref. [28].
[48] D. Y. Qiu, T. Cao, and S. G. Louie, Phys. Rev. Lett. **115**, 176801 (2015).
[49] D. MacNeill, C. Heikes, K. F. Mak, Z. Anderson, A. Kormányos, V. Zólyomi, J. Park, and D. C. Ralph, Phys. Rev. Lett. **114**, 037401 (2015).
[50] A. Srivastava, M. Sidler, A. V. Allain, D. S. Lembke, A. Kis, and A. Imamoğlu, Nat. Phys. **11**, 141 (2015).
[51] G. Aivazian, Z. Gong, A. M. Jones, R.-L. Chu, J. Yan, D. G. Mandrus, C. Zhang, D. Cobden, W. Yao, and X. Xu, Nat. Phys. **11**, 148 (2015).
[52] M. V. Durnev and M. M. Glazov, Phys. Rev. B **93**, 155409 (2016).
[53] J. P. Perdew and A. Zunger, Phys. Rev. B **23**, 5048 (1981).
[54] F. A. Rasmussen and K. S. Thygesen, J. Phys. Chem. C **119**, 13169 (2015).
[55] W. S. Yun, S. W. Han, S. C. Hong, I. G. Kim, and J. D. Lee, Phys. Rev. B **85**, 033305 (2012).
[56] A. D. Corso, Computational Materials Science **95**, 337 (2014).
[57] R. Bistritzer and A. H. MacDonald, PNAS **108**, 12233 (2011).